Nano Research

Open Access

Research Article

Synergistic Co_2O_3/Bi_2O_3 co-doping in MnZn ferrites for ultra-low magnetic noise shielding in quantum precision measurements

Bowen Sun[1] ✉, Yueyang Zhai[1,2], Sateesh Bandaru[3], Tianshi Cheng[1], Yongsen Huang[1], Kun Chen[1], Shiqiang Zheng[1,2], Bangcheng Han[1,2], Jianli Li[1,2], Danyue Ma[1,2] ✉, Fan Wu[4] ✉, and Wenhuan Huang[5] ✉

[1] *School of Instrumentation and Optoelectronic Engineering, Beihang University, Beijing 100191, China*
[2] *Hefei National Laboratory, Hefei 230088, China*
[3] *Institute of Advanced Magnetic Materials, College of Materials and Environmental Engineering, Hangzhou Dianzi University, Hangzhou 310012, China*
[4] *State Key Laboratory of Advanced Materials for Intelligent Sensing, Department of Chemistry, School of Science & Institute of Molecular Aggregation Science, Tianjin University, Tianjin 300072, China*
[5] *Key Laboratory of Chemical Additives for China National Light Industry, College of Chemistry and Chemical Engineering, Shaanxi University of Science and Technology, Xi'an 710021, China*

Cite this article: *Nano Research*, **2026**, *19*, 94908875. https://doi.org/10.26599/NR.2026.94908875

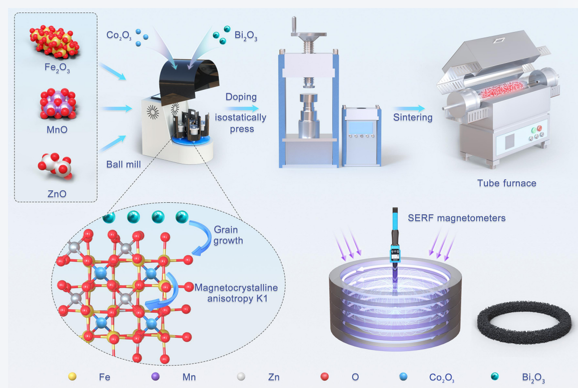

ABSTRACT: MnZn ferrite, characterized by the low power loss, the high electrical resistivity, and the high magnetic permeability, is a promising candidate for the low-noise magnetic shielding applications. However, as the dissipative material, MnZn ferrites inherently generate a magnetic noise, which fundamentally limits the sensitivity of the magnetometers operating in the spin-exchange relaxation-free (SERF) regime. Herein, we report a synergistic co-doping strategy using Co_2O_3 and Bi_2O_3 to effectively suppress the intrinsic magnetic noise of MnZn ferrites. By systematically tuning the concentrations of Co_2O_3 and Bi_2O_3, the power loss, complex magnetic permeability, and microstructural evolution of undoped, singly doped, and co-doped MnZn ferrites are comprehensively investigated. Notably, co-doping with 1600 ppm Co_2O_3 and 400 ppm Bi_2O_3 reduces the low-frequency magnetic noise by more than 50%, which is attributed to refined grain boundary structures and suppressed hysteresis losses. The optimized MnZn ferrite is further employed to fabricate a magnetic shield for a SERF magnetometer, achieving a single-channel sensitivity of 0.25 $fT/Hz^{1/2}$. This study paves an effective materials-engineering route to minimize magnetic noise in ferrite-based shielding systems, providing a solid foundation for the development of next-generation ultra low-noise platforms for the quantum precision measurements.

KEYWORDS: MnZn ferrite, Co_2O_3/Bi_2O_3, co-doping, intrinsic magnetic noise, magnetic shielding materials, SERF magnetometer, quantum precision measurement

1 Introduction

Magnetic field is one of the most important physical quantities in understanding the universe [1]. To measure the magnetic fields with an ultra-high precision, various magnetic sensors are developed. Among them, atomic magnetometers operating in the spin-exchange relaxation-free (SERF) regime have achieved sub-femtotesla ($fT/Hz^{1/2}$) sensitivity, becoming the most sensitive magnetic field detection technology to date [1–4]. In the SERF magnetometers, the alkali vapor is enclosed within a magnetic shielding, in which the alkali atoms' spin-exchange collision frequency far exceeds their Larmor precession frequency [5]. This allows a rapid spin exchange in alkali atoms while maintaining a collective spin coherence, thereby enhancing the sensitivity of magnetic measurement. The ultra-small external magnetic field is measured by monitoring the probe beam's polarization rotation.

Received: February 12, 2026; **Revised:** May 6, 2026
Accepted: May 26, 2026

✉Address correspondence to Bowen Sun, sunbowen1996@buaa.edu.cn; Danyue Ma, madanyue0419@buaa.edu.cn; Wenhuan Huang, huangwenhuan@sust.edu.cn; Fan Wu, wufan0817@tju.edu.cn

Due to a high sensitivity, SERF magnetometers have become an advanced non-invasive technique to measure weak biomagnetic signals [6] and neuronal electrical activity in the brain [7]. However, SERF magnetometers have not achieved the theoretical sensitivity due to the magnetic noise generated by the magnetic shielding materials that can mask the signal of magnetic field [1].

According to the fluctuation dissipation theorem, the magnetic noise of magnetic shielding materials can be represented by the power loss of materials [8, 9]. Within the typical frequency of SERF magnetometers (< 200 Hz), the magnetic noises are primarily aroused from two mechanisms: eddy current loss and hysteresis loss [10, 11]. MnZn ferrites, with a high magnetic permeability and electrical resistivity, can effectively suppress the eddy current loss [12, 13] and are thus promising candidates for reducing the noise of magnetic shielding system [14, 15]. Lee et al. derived the expression of eddy current magnetic noise of a finite-length cylindrical magnetic shielding.

$$\delta B_{e}=\frac{\mu_{0}\sqrt{\sigma G t}}{r}\sqrt{\frac{2}{3\pi}kT} \tag{1}$$

where r is the radius of ferrite shielding, t is wall thickness, T is temperature, G is the shape factor, G = 0.657, 0.460, and 0.438 when the aspect ratio equals to 1, 1.5, and 2. For MnZn ferrite materials, the typical value of electrical conductivity is ~ 0.13 S/m. When the radius of magnetic shield is 57 mm, thickness is 10 mm, and aspect ratio is 2, calculated eddy current magnetic noise at the room temperature is 0.03 fT/Hz$^{1/2}$, which is much smaller than the hysteresis magnetic noise at low frequency. However, when there was an electronic interference, the hysteresis loss—resulting from phase lag in magnetic domain responses—remains unavoidable, causing the hysteresis-induced magnetic noise to be the dominant limitation for ferrite-based magnetic shields [16].

The magnetic noise of the ferrite shield is treated as an effective electronic element of the pickup coil. By applying the fluctuation-dissipation theorem, the voltage fluctuation at the coil terminals is expressed as

$$S_{v}(f)=4kTR_{\mathrm{eff}}(f) \tag{2}$$

where k is Boltzmann constant, R_{eff} is the effective resistivity, T is temperature and f is the frequency, and the time-averaged power dissipation is a product of the oscillating current and the effective resistance

$$P(f)=\frac{1}{2}I^{2}R_{\mathrm{eff}}(f) \tag{3}$$

where I is an oscillating current of the pickup oil. By combining these equations, the magnetic field noise can be expressed as

$$\delta B(f)=\frac{\sqrt{4kT}\sqrt{2P(f)}}{ANI\omega} \tag{4}$$

Thus, the intrinsic magnetic noise originates from the dissipation power of the ferrite, including eddy current loss $P_{\mathrm{eddy}}=\int\frac{1}{2}\sigma E^{2}\mathrm{d}V$ and hysteresis loss $P_{\mathrm{hyst}}=\int\frac{1}{2}\omega\mu'' H^{2}\mathrm{d}V$. Since the magnetic noise of ferrite shield is mainly due to the hysteresis loss [17], magnetic noise can be expressed as [18]

$$\delta B(f)=\frac{\sqrt{4kT}\sqrt{\int\mu'' H^{2}\mathrm{d}V}}{ANI\sqrt{\omega}} \tag{5}$$

where H is the magnetic field intensity generated by a current I flowing through coil. H is calculated numerically using a finite element analysis software (MAXWELL 3D). By solving the electrostatics problem for a finite-long hollow cylinder, Kornack et al. showed that the longitudinal magnetic field noise on the axis of the shield is [10]

$$\delta B_{\mathrm{magn}}=\frac{0.26\mu_{0}}{r\sqrt{t}}\sqrt{\frac{4kT\mu''}{\omega\mu'^{2}}} \tag{6}$$

where r is radius, t is the thickness, T is temperature, $\mu'$and μ'' are the real and imaginary parts of complex magnetic permeability. Assuming a ferrite magnetic shielding with a constant magnetic permeability, the hysteresis noise contribution of a magnetic shielding is proportional to the squared root of μ''/μ'^2. Kornack et al. analyzed the hysteresis magnetic noise of a ferrite magnetic shielding using the power dissipation theorem [18]. Shen et al. used this model to analyze the magnetic noise of the cobalt-based amorphous alloy and μ-metal magnetic shields respectively [19]. To improve the estimation accuracy of magnetic noise, Yang et al. improved the magnetic permeability measurement method at the low frequencies using the hysteresis model [20]. All these studies above provided a theoretical insight for modeling magnetic noises, yet few have experimentally reduced the magnetic noise through a microstructural or compositional design of the MnZn ferrites.

According to a proportionality between a square root of μ''/μ'^2 and the magnetic noise, an increment of μ' and a decrement of μ'' are essential in minimizing the hysteresis-induced magnetic noise. In a polycrystalline MnZn ferrite, the cations are distributed in the octahedral (A) and tetrahedral (B) sites, and this cation distribution modulates a A–O–B super-exchange interaction, which modulates the magnetic permeability of ferrite materials [21]. Several works have been carried out to improve the magnetic performances of ferrites [22, 23]. The main strategies can be classified as two ways. (1) Thermal control: by optimizing the sintering temperature to enhance a grain growth and increase the initial permeability of ferrites [24, 25]. (2) Chemical modification: by doping the metallic oxide which can tailor the electromagnetic properties. For example, Bi_2O_3 is a sintering promoter due to its low melting point, and doping Bi_2O_3 can promote a liquid-phase sintering and enhance ferrites' saturation induction B_S [26, 27]. On the other hand, doping Co_2O_3 which changes magnetocrystalline anisotropy [28] could improve the frequency stability of ferrites [29, 30]. For other dopants, such as CaO and SiO_2 could form the resistive grain boundaries [31], reducing the eddy current loss [32, 33]. These studies have mainly focused on improving the magnetic properties, while the synergistic effect of multi-ion doping on the magnetic noise suppression—a key determinant of SERF magnetometer sensitivity—remains largely unexplored.

In this work, we systematically investigate the synergistic effects of Co_2O_3 and Bi_2O_3 co-doping on the magnetic noise and microstructural evolution of MnZn ferrites. By precisely optimizing the doping concentrations, the magnetic noise is reduced by over fivefold compared to the undoped MnZn ferrite, while the frequency stability is significantly enhanced. These improvements are attributed to a grain growth facilitation and a refined magnetic moment distribution of Co cations at the octahedral sites. This work establishes a rational pathway to engineer low-noise soft magnetic MnZn ferrites, paving a way for the development of next-generation magnetic shielding materials for quantum precision measurements.

2 Results and discussion

2.1 Microstructures of Co_2O_3/Bi_2O_3 Co-doped MnZn Ferrites

MnZn ferrites were synthesized via a solid-state reaction, in which stoichiometric raw powders were ball-milled and doped with different amounts of CaO, SiO_2, Bi_2O_3, and Co_2O_3. For sample nomination, the number after elements' abbreviation represents doping amount (in hundreds). For example, C18Bi4 represents the doping amount of Co is 1800 ppm and the doping amount of Bi is 400 ppm (Table S1 in the Electronic Supplementary Material (ESM)). In this work, Bi_2O_3 is a low melting point additive and can promote samples' grain growth, which is advantageous for increasing the real magnetic permeability μ'. Co_2O_3 could compensate the overall K_1 in the sample and would enter MnZn ferrite's crystalline lattice to reduce the power loss. After the doping, the powders were isostatically pressed into a toroidal shape with a height of 4 mm, an inner diameter of 8 mm and an outer diameter of 10 mm for the sintering process. The toroidal MnZn ferrites samples are used to investigate the synergic effects of co-doped Co_2O_3/Bi_2O_3@MnZn in suppressing the magnetic noise. After determining the composition, a cylindrical magnetic shielding with an outer diameter of 270 mm, an inner diameter of 210 mm, and a height of 375 mm was made to provide an ultra-low magnetic noise environment for SERF magnetometry.

The morphologies of singly doped and co-doped MnZn ferrites are illustrated in Fig. 1. The intragranular and intergranular pores are formed in all sample, as shown in Figs. 1(a)–1(d). This is attributed to the sintering-induced cationic vacancies, which promote the inhomogeneous grain growth [34]. When doping amount of Co_2O_3 increases from 0 to 1200 ppm, the average grain size of MnZn ferrites increases from 40.7 to 48.9 μm, as shown in Fig. 1(e). Meanwhile, the grain size gradually increases with the

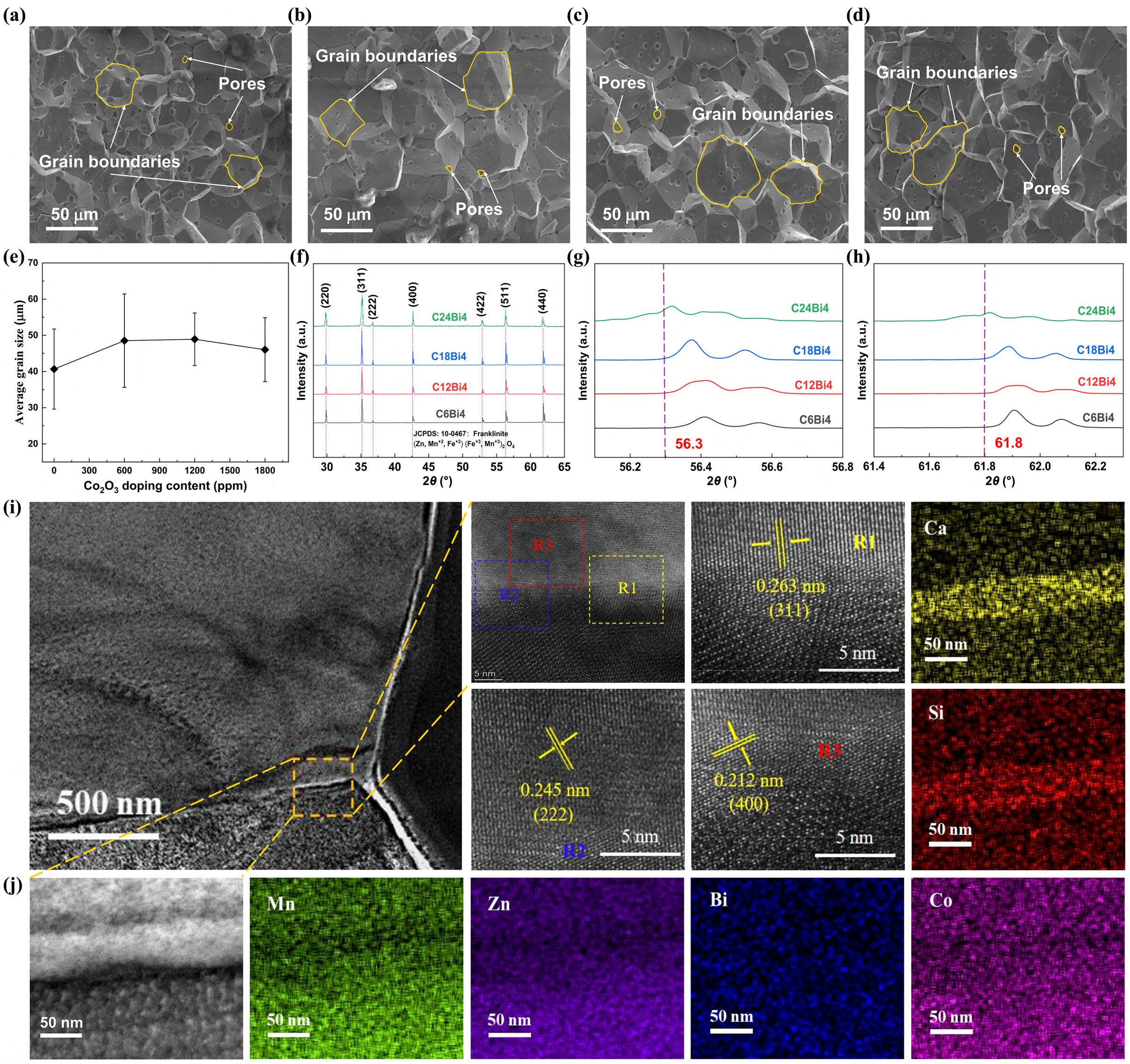

Figure 1 Microstructure and crystallography phase characterization of the co-doped MnZn ferrites. (a)–(d) SEM images of cross-sectional region of ferrite samples doped with 400 ppm Bi_2O_3 when the addition of Co_2O_3 is 0, 600, 1200, and 1800 ppm. (e) The average grain sizes of MnZn ferrites under different Co_2O_3 doping amount. (f)–(h) The XRD spectra of MnZn ferrites, enlarging view for high-angle region of (511) and (440). (i) HAADF for MnZn ferrite doped with 1800 ppm of Co_2O_3 and 400 of ppm Bi_2O_3. (j) EDS maps of the regions near the grain boundary.

sintering temperature (Fig. S1 in the ESM) and the grain size's standard deviation of the sample doped with 600 ppm Co_2O_3 is the largest (Fig. S2 in the ESM). The uneven distribution is due to inconsistent grain migrations during the heat preservation process [35].

In Fig. 1(f), XRD patterns of MnZn ferrites affirm a Franklinite phase structures with a space group of $Fd\bar{3}m$, according to the standard JCPDS card No. 10-0467. The shoulder peak observed in the XRD pattern may be attributed to the Cu Kα_2 splitting. During the sintering process, Co_2O_3 is reduced to Co^{2+} under a low oxygen partial pressure. Since Co^{2+} ions have a strong preference for the octahedral sites [36], they preferentially substitute for Fe^{3+} ions located at octahedral positions within the spinel structure, which results in an increase in the lattice constant [37] and a consequent decrease of 2θ angle, as shown in Figs. 1(g) and 1(h). In an intergranular junction between two neighboring grains, the interplanar spacings of 0.263, 0.245, and 0.212 nm corresponding to [311], [222], and [400] confirm a spinel crystalline of Franklinite ferrite (Fig. 1(i)). From EDS maps in the linear junction (Fig. 1(j)), the grain boundary layer was observed with a segregation of Ca/Si, which weakens the magnetic exchange coupling at grain-boundary regions and reduce the power loss [12]. The power loss of ferrites is dominant by the hysteresis loss P_h and the eddy current loss P_e [38, 39]. The formed Ca/Si enriched boundary layer has a high resistivity and therefore reduces the eddy current loss, which explains a reduced power loss observed in C18Bi4@MnZn [40].

2.2 Electromagnetic parameters of Co_2O_3/Bi_2O_3 co-doped MnZn ferrites

The complex permeability of undoped, singly doped and co-doped MnZn ferrite was measured by an improved impendence method to determine the optimal doping amount of Co_2O_3 and Bi_2O_3 for magnetic noise suppression over the typical working frequency of SERF magnetometry. The real part of the complex permeability μ' is expressed as $\mu' = 1 + \chi_{spin} + \chi_{dw}$, where χ_{spin} and χ_{dw} represent the magnetic susceptibility due to the spin rotation and domain wall movements [41]. At low frequencies, the magnetization of MnZn ferrites is dominated by domain wall movements, which are closely related to materials' microstructures. For instance, the presence of pores hinders the domain wall motions and cause magnetic permeability μ' to decrease [42].

The magnetic permeability of MnZn ferrites singly doped with Bi_2O_3 is analyzed. The real part of the complex magnetic permeability μ' decreases with Bi_2O_3 additions, which because Bi_2O_3 doping introduce the intragranular and intergranular pores [33], which impede domain wall motion (Fig. S4(a) in the ESM). The magnetic permeability μ' doesn't reduce much with Bi_2O_3 doping amount (Fig. S4(b) in the ESM). In Fig. 2(a), μ' of singly doped Bi@MnZn ferrites decreases with frequencies, which could be attributed to resistance of wire at low frequency [20]. In Fig. 2(b), the imaginary part of complex permeability μ'' decreases with the Bi_2O_3 doping amount. This might due to Bi_2O_3 doping promotes the formation of a highly resistive grain boundary, which weakens the pinning effect of domain wall and reduces the imaginary part of the complex permeability [43]. In Fig. 2(c), the effects of Bi_2O_3 on the power loss were analyzed. It is found that samples doped with 400 ppm Bi_2O_3 have the minimal P_{cv} of 0.98 kW/m^3 at 30 Hz, which corresponds to the calibration frequency of SERF magnetometer. P_{cv} varies with Bi_2O_3 addition and increases with the magnetic flux density, as shown in Fig. 2(c). The minimum P_{cv} value of 1.83 kW/m^3 is observed in samples doped with 400 ppm Bi_2O_3 at 0.03 T, which indicates the MnZn ferrites under this doping strategy would yield the smallest magnetic noise according to Eq. (4). In previous study, power loss of MnZn ferrite has been extensively studied for high frequency applications [44, 45], but the modulation of power loss below 100 Hz has been rarely studied.

Co_2O_3 has a large magnetocrystalline anisotropy and can significantly improve the frequency dependence of ferrites [33]. As shown in Figs. 2(d) and 2(e), Co_2O_3 doping increases μ' and improves the spectra stability of magnetic permeability. This is attributed to an incorporation of Co^{2+} into the spinel lattice of MnZn ferrites that modulate the magnetization of materials [46]. Co^{2+} have a negative magnetocrystalline anisotropy K_1 and they could compensate the positive anisotropy of Fe^{2+} when the doping amount of Co_2O_3 increases, resulting in a net $K_1 = 0$, which reduces the domain rotation and domain wall motion, leading to a decrease in μ'', as shown in Fig. 2(e).

To examine synergic effects of Co_2O_3/Bi_2O_3 doping on magnetic noise, μ''/μ'^2 are calculated according to Eq. (3). In Fig. 2(g), μ''/μ'^2 increase with frequency and decrease with Bi_2O_3 addition, reaching to the minimum at 400 ppm. This is consistent with measured power loss in Fig. 2(c). The comparison of μ''/μ'^2 shows the addition of Co_2O_3/Bi_2O_3 reduces μ''/μ'^2 by more than a half at low frequencies, as shown in Fig. 2(h). Overall, 1800 ppm of Co_2O_3 and 400 ppm of Bi_2O_3 is the optimal doping amount to suppress the magnetic noise.

2.3 Magnetic shielding performance and mechanism studies

First principles calculation is performed to explain the improved magnetic properties observed in the sample of C18Bi4@MnZn. The settlement of Co_2O_3 at the lattice sites of grain matrix could modify the electron hopping of MnZn ferrite and thus improve its magnetic properties [28]. In first principal calculation, the models of MnZn ferrite with Co ions at octahedral (A) stie and tetrahedral (B) site are given in the Model A and B, as shown in shown in Fig. 3. Density of states (DOS) is calculated to analyze the electrochemical stability of different models. The electrons number at Fermi level for Model A and B are 0 and 14.48 electronic states/eV respectively, as shown in Figs. 3(b) and 3(d). Less electronical states at Fermi level indicates more stable structure and higher electrochemical stability, so 3d electrons of Co^{3+} tend to occupy octahedral sites [47]. In ferrimagnetic materials, assuming the magnitude of moment remains constant, the magnetization can be expressed as

$$M = \int N\mu\cos\theta p(\theta, T, B) = N\mu \frac{\int_0^\pi e^{\mu B\cos\theta/k_B T}\cos\theta\sin\theta d\theta}{\int_0^\pi e^{\mu B\cos\theta/k_B T}\sin\theta d\theta} \quad (7)$$

where μ is the magnetic moment, N is number of magnetic moments per volume, p is the probability for a moment to have an orientation angle in an interval of $[\theta, \theta + d\theta]$. The integration yields

$$M = N\mu\left[\coth\left(\frac{\mu B}{k_B T}\right) - \frac{k_B T}{\mu B}\right] = N\mu L(x) \quad (8)$$

where $x = \mu_B/k_B T$, and the Langevin function $L(x) = \coth(x) - 1/x$, when x is small at a small B, $L(x) \approx x/3$, the magnetization becomes

$$M = \frac{N\mu x}{3} = \frac{N\mu^2 B}{3k_B T} \quad (9)$$

Recall that $B = \mu_0 H$, the magnetic susceptibility can be given by

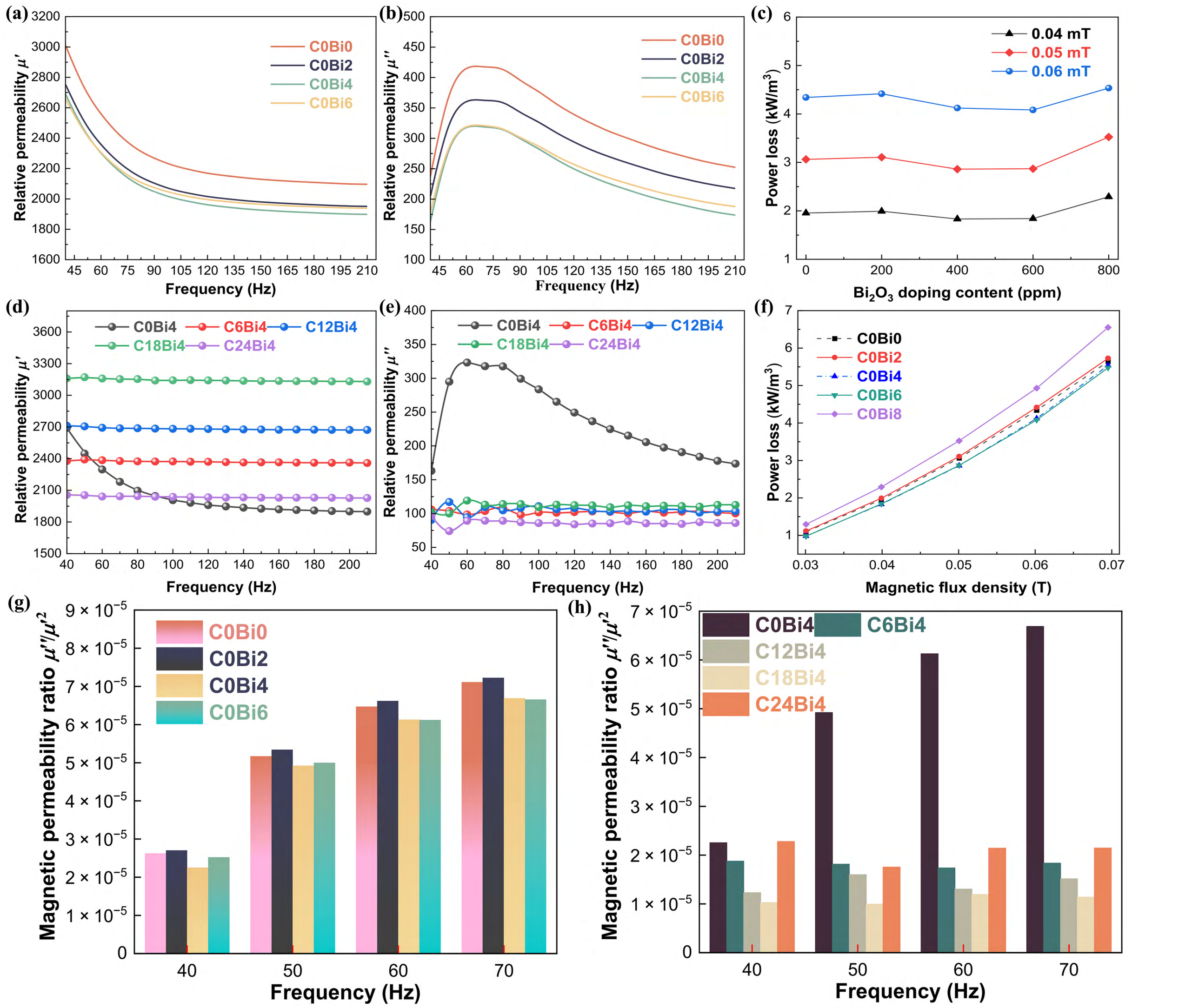

Figure 2 Magnetic properties of the undoped, singly doped and co-doped MnZn ferrites. (a) and (b) The real and imaginary part of complex permeability of Bi_2O_3 doped samples. (c) The power loss of samples with different Bi_2O_3 addition at 30 Hz. (d) and (e) The real and imaginary part of complex permeability of Co_2O_3/Bi_2O_3 co-doped samples. (f) The power loss of samples under different magnetic field. (g) μ''/μ'^2 of samples doped with Bi_2O_3 under 100 Hz. (h) μ''/μ'^2 of samples co-doped with Co_2O_3/Bi_2O_3 under 100 Hz.

$$\chi = \frac{M}{H} = \frac{\mu_0 M}{B} = \frac{\mu_0 N \mu^2}{3k_B T} \tag{10}$$

The occupancy of 3d orbitals in Co^{3+} ions is governed by a local symmetry. For the octahedral and tetrahedral ligand fields, the degeneracy is lifted, creating an energy gap between the t_{2g} states (d_{xy}, d_{xz}, d_{yz}) and eg states (d_{z^2}, $d_{x^2-y^2}$). The octahedral complexes of Co^{3+} exhibit an observed high-spin moment of 5.1–5.7, while reduced splitting in the tetrahedral complexes gives an observed moment of 4.2–4.8 [48]. Such increment of moment gives rise of the magnetic susceptibility, which explained increased magnetic permeability μ' in the sample of C18Bi4@MnZn.

The magnetic domain of C18Bi4@MnZn is observed by an in-situ Lorentz TEM to analyze the hysteresis loss of MnZn ferrites. The *in-situ* Lorentz TEM characterization of un-doped MnZn ferrites was conducted (Fig. S3 in the ESM). In Fig. 4, the magnetic domain walls begin to move under an applied magnetic field. Since MnZn ferrites have a low coercivity and a small saturation magnetization [49], the applied magnetic fields from 0 to 50 to −50 mT are chosen to investigate the domain wall movements, as shown in Fig. 4(a). It is observed that applied field will induce an opposite direction of change in the normalized areas at 50 and −50 mT, indicating the irreversible domain wall movements occur when external fields are applied and such irreversible wall movements can cause the hysteresis loss in the ferrite magnetic shielding [50], introducing a magnetic noise into the system, as shown in Figs. 4(b)–4(e). When the external field is below 30 mT, the magnetic domain wall movements are mainly reversible type. To examine the effectiveness of C18Bi4@MnZn ferrite in suppressing the magnetic noise, a SERF magnetometer based on potassium sensing unit is used. By optimizing oxygen content during the sintering process, the magnetic permeability of C18Bi4@MnZn ferrite achieved the permeability μ'/μ_0 = 13,909, μ''/μ_0 = 258. In this atomic magnetometer, the atomic spin executes a Larmor precession in an external magnetic field, and the rate of Larmor precession can be expressed as

$$\omega = \gamma \cdot |B| \tag{11}$$

where γ is gyromagnetic ratio of alkali atoms, ω is the angular

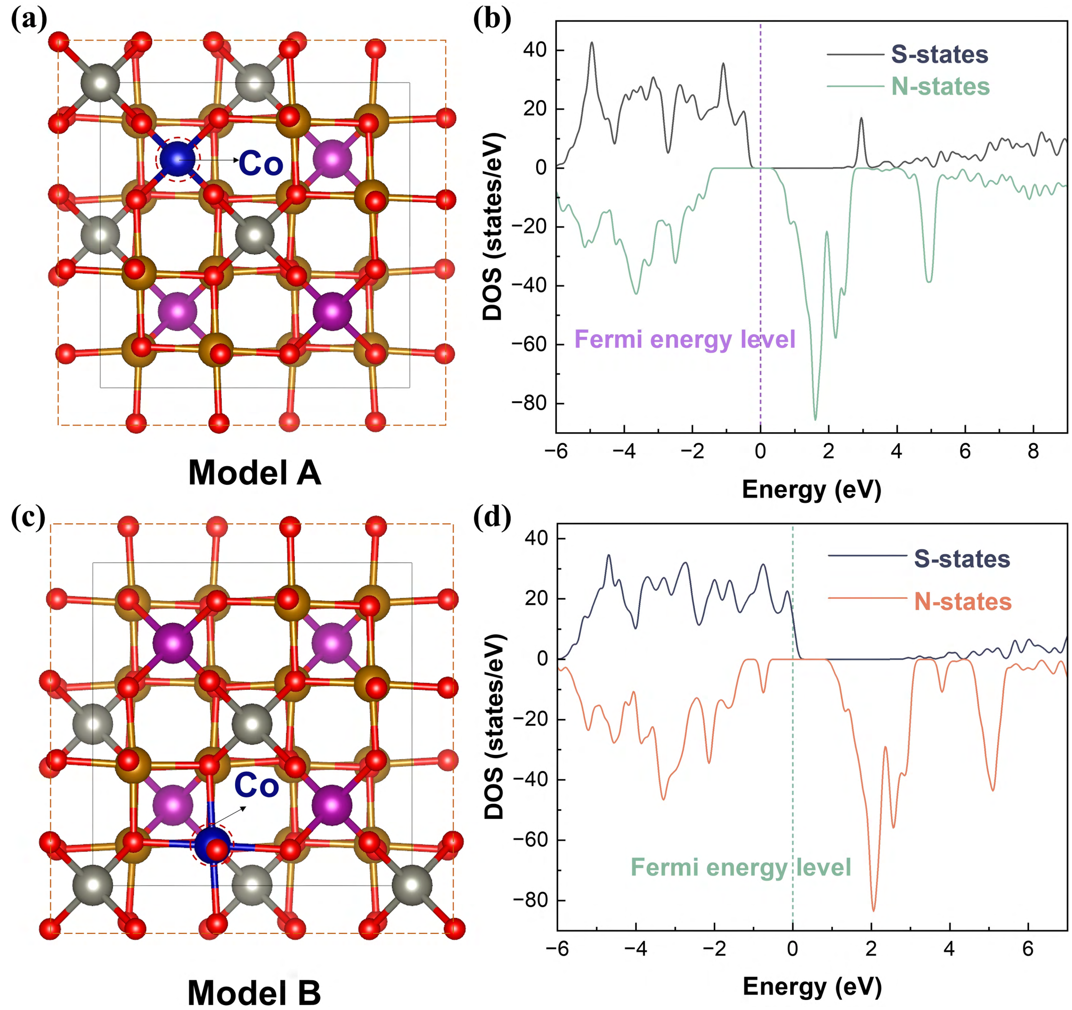

Figure 3 First-principles calculation of co-doped MnZn ferrites. (a) The model of Co ions at octahedral sites. (b) Calculated DOS of Co at octahedral sites. (c) The model of Co ions at tetrahedral sites. (d) Calculated DOS of Co at octahedral sites.

frequency, B is external magnetic field. In a natural state, the spin direction of K atoms is randomly distributed. To makes the K atoms spin in the same direction, a circularly polarized light in the D_1 transition line of K atoms (770.108 nm) is pumped to polarize K atoms in a nearly zero field environment. The linearly polarized light in the D_2 transition line of K atoms (769.8 nm) is used to probe the atoms' rotation angle under the external magnetic field. By measuring the rotation angle, a slight change in the magnetic field can be determined. During the magnetic measurement, the atomic ensemble is heated to 200 °C to achieve a high atomic number density of (10^{13}–10^{15}) [1]. The evolution of atomic spin with light and magnetic field can be described by a density matric equation

$$\frac{\mathrm{d}}{\mathrm{d}t}\rho = \frac{1}{i\hbar}[\mathcal{H},\rho] + \frac{1}{T_{\mathrm{SE}}}\left[(1+4\langle S\rangle\cdot S)-\rho\right] + R_{\mathrm{rel}}[-\rho] + R_{\mathrm{OP}}\left[(1+2s\cdot S)-\rho\right] + D\nabla^2\rho \tag{12}$$

where D is diffusivity, S is spin vectors, T_{SE} is spin relaxation time, R_{op} is relaxation rate of pump light, R_{rel} is total relaxation, and φ is the nuclear part in matrix. Then, the evolution of average angular momentum <F> of atomic ensemble can be expressed as

$$\frac{\mathrm{d}\langle F\rangle}{\mathrm{d}t} = Tr\left[\frac{\mathrm{d}\rho_{\mathrm{g}}}{\mathrm{d}t}F\right] + Tr\left[\frac{\mathrm{d}\rho_{\mathrm{ex}}}{\mathrm{d}t}F\right] = \gamma_{\mathrm{B}}B\times\langle S\rangle \tag{13}$$

where ρ_{g} and ρ_{ex} are the density populations at the ground state and excited state and B is external magnetic field. By analyzing the density population of two-level system in alkali atomic ensemble, the magnetic field can be determined.

A magnetic shield made of C18Bi4@MnZn ferrite is fabricated. In the magnetic shielding, the magnetic field gradient is 0.03 nT/cm along the x-axis, 0.1 nT/cm along the y-axis, and 0.09 nT/cm along the z-axis (Fig. S5 in the ESM). Before the magnetic field measurement, the optical depth of vapor cell in SERF magnetometer is optimized (Fig. S8 in the ESM) and sensor's frequency response is analyzed to convert the electric signal of photodetectors into the magnetic signals (Table S2 in the ESM). It is found the electron spins will respond when there was an external magnetic field along the y direction of the vapor cell (Fig. S7 in the ESM). In Fig. 5(a), the sensitivity of magnetometer from a single channel and from the gradient measurement are given. The magnetic measurement inside C18Bi4@MnZn magnetic shield reveals a single-channel sensitivity of 0.25 fT/Hz$^{1/2}$ at 46 Hz, which was calibrated using a sinusoidal magnetic field of 10 pT, which was generated by a coil with a known coil's constant (Fig. S9 in the ESM). By recording the system's amplitude-frequency response

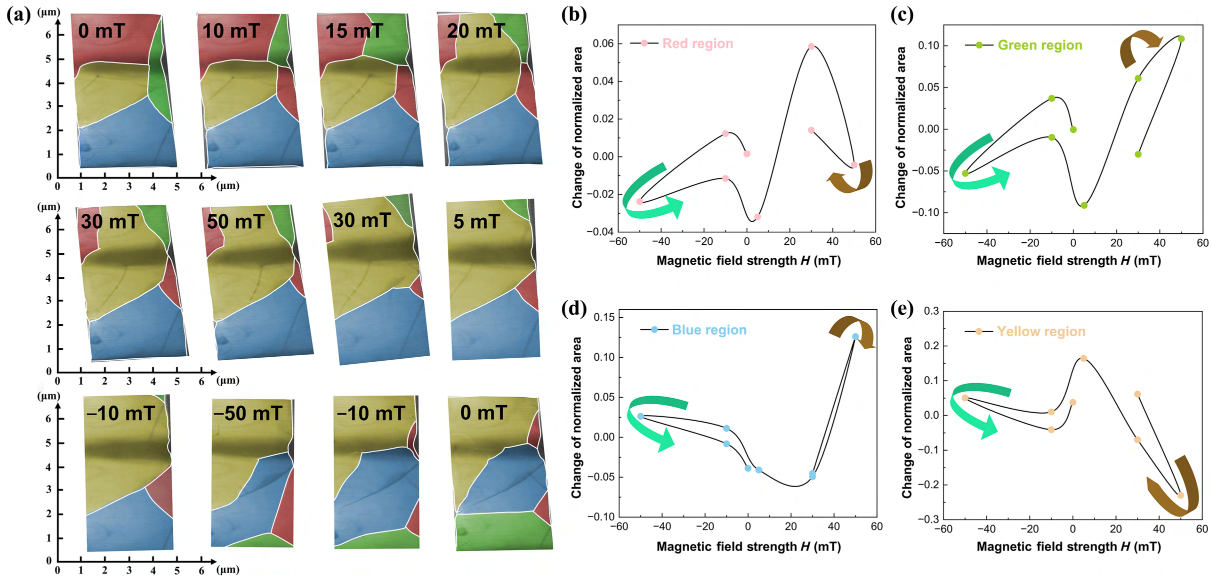

Figure 4 Characterization of C18Bi4@MnZn with external fireld from −50 to 50 mT. (a) *In-situ* Lorentz TEM. Domain walls are referred by white lines. Change of normalized domain areas: (b) red region, (c) green region, (d) blue region, and (e) yellow region.

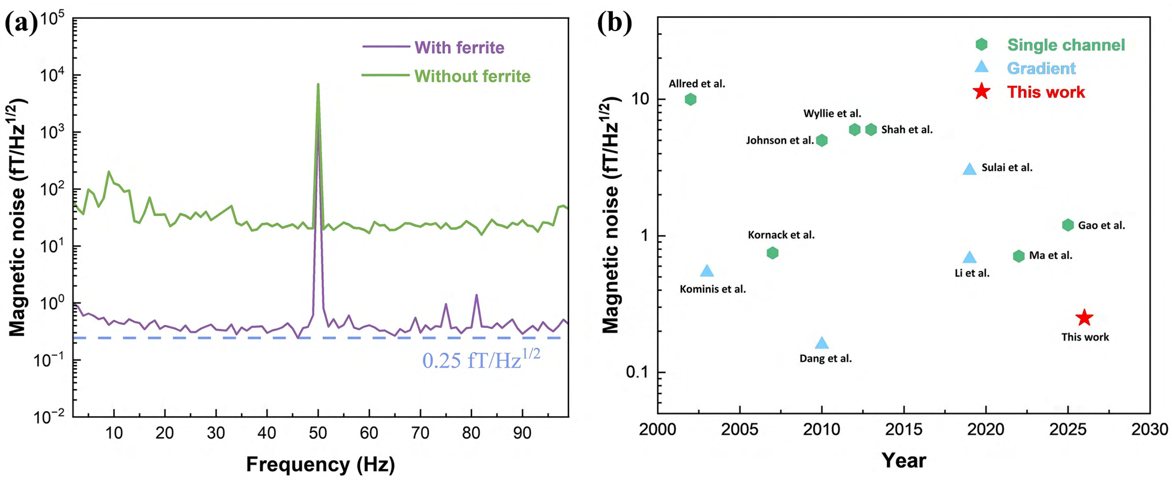

Figure 5 Sensitivity of SERF magnetometer. (a) Magnetic noise with and without the ferrite magnetic shielding. (b) The comparison of magnetic noise of C18Bi4@MnZn ferrites and previously reported works [11, 18, 51–59].

from 5 to 100 Hz using a lock-in amplifier. The output voltage spectral density was converted to magnetic field spectral density using the measured responsivity (Table S2 in the ESM). The sensitivity of 0.25 $fT/Hz^{1/2}$ was taken as the minimum noise floor below 100 Hz. The poor sensitivity when there was no ferrite shield is attributed to the large dissipative power loss of highly permeable permalloy [57]. In the experiment, the magnetic noise of ferrite magnetic shield was deconvoluted from the photon shot noise and spin projection noise by adjusting probe intensity, and it is found sensitivity cannot be significantly improved by adjusting the probe beam's intensity, indicating the performance of the magnetometer is not limited by the noise from lasers. C18Bi4@MnZn ferrites significantly reduce the magnetic noise and improves sensitivity. The prominent noise peak at 50 Hz is originated from a power-line frequency harmonic interference. In SERF magnetometry, a high-density alkali vapor is enclosed within the magnetic shield. To achieve the required vapor density, the vapor cell is heated using a heating film driven by the power line, which introduces the prominent noise at 50 Hz. Although MnZn ferrite shield can effectively suppress the external magnetic noise, it cannot attenuate internal power-line frequency harmonic interference arising from the vapor cell heating. In Fig. 5(b), SERF magnetometer in this study is much more sensitive than the previous works， which is due to reduce the magnetic noise that is attributed to the synergistic doping effects of Co_2O_3 and Bi_2O_3 in complex magnetic permeability, microstructures and power loss characteristics in MnZn ferrites. Meanwhile, C18Bi4@MnZn ferrite magnetic shielding has an average shielding coefficient of 1221 in *x* direction and 1102 in *y* direction (Fig. S6 in the ESM). The variation of shielding coefficient in each direction could be caused by magnetic field fluctuations in the environment.

3 Conclusion

In conclusion, this work systematically elucidates the synergistic effects of Co_2O_3 and Bi_2O_3 co-doping on the magnetic properties and microstructural evolution of MnZn ferrites. By precisely optimizing the doping ratio to 1600 ppm Co_2O_3 and 400 ppm

Bi_2O_3, the intrinsic magnetic noise is reduced by more than 50% compared with undoped ferrites, particularly in the low-frequency regime. Detailed analyses reveal that the suppression of magnetic noise originates from refined grain boundary structures and reduced hysteresis losses, highlighting the critical role of microstructure engineering in dissipative magnetic shielding materials. When applied as a magnetic shielding material for a SERF magnetometer, the optimized MnZn ferrite enables a single-channel magnetic field measurement sensitivity of 0.25 $fT/Hz^{1/2}$, outperforming previously reported ferrite-based shielding systems. Beyond performance enhancement, this study clarifies the microscopic origins of magnetic noise in MnZn ferrites and provides a feasible and generalizable strategy for engineering low-noise magnetic shielding materials, advancing the development of quantum sensing and precision measurement technologies. To further reduce the magnetic noise, a controlled microstructure and engineered grain boundaries which reduce the domain wall mobility could be studied.

Electronic Supplementary Material: Supplementary material (experimental procedures, materials characterizations, data analyses, theoretical principles of SERF magnetometry, and supporting figures/tables for MnZn ferrites used in ultra-low magnetic noise shielding) is available in the online version of this article at https://doi.org/10.26599/NR.2026.94908875.

Data availability

All data needed to support the conclusions in the paper are presented in the manuscript and the Electronic Supplementary Material. Additional data related to this paper may be requested from the corresponding author upon request.

Acknowledgements

This work was supported by the China Postdoctoral Science Foundation (No. 2025M784277), the National Natural Science Foundation of China (Nos. 42388101 and 62203028), and Innovation Program for Quantum Science and Technology (No. 2021ZD0300501). We would like to extend our appreciation to Prof. Guohua Bai, Prof. Zhenhua Zhang and Prof. Xiaolian Liu from Hangzhou Dianzi University for many valuable suggestions on the TEM characterization.

Declaration of competing interest

All the contributing authors report no conflict of interests in this work.

Author contribution statement

B. W. S. conceived study, designed the experiments, collected and analyzed SEM and TEM data, and wrote the original draft of the manuscript. Y. Y. Z. and D. Y. M. supervised the research and provided experimental resources. S. B. developed the first-principal calculation model and performed DFT analysis. T. S. C., Y. S. H., and K. C. conducted the data investigation and assisted in visualization. S. Q. Z., B. C. H., and J. L. L. are the project administrators and provide experimental resources. F. W. and W. H. H. edited the manuscript and revised it.

Use of AI statement

None.

References

[1] Kominis, I. K.; Kornack, T. W.; Allred, J. C.; Romalis, M. V. A subfemtotesla multichannel atomic magnetometer. *Nature* **2003**, *422*, 596–599.

[2] Bloch, I. M.; Shaham, R.; Hochberg, Y.; Kuflik, E.; Volansky, T.; Katz, O. Constraints on axion-like dark matter from a SERF comagnetometer. *Nat. Commun.* **2023**, *14*, 5784.

[3] Qin, Y. S.; Shao, Z. H.; Hong, T. Z.; Wang, Y. H.; Jiang, M.; Peng, X. H. New classes of magnetic noise self-compensation effects in atomic comagnetometer. *Phys. Rev. Lett.* **2024**, *133*, 023202.

[4] Wu, T.; Blanchard, J. W.; Centers, G. P.; Figueroa, N. L.; Garcon, A.; Graham, P. W.; Kimball, D. F. J.; Rajendran, S.; Stadnik, Y. V.; Sushkov, A. O. et al. Search for axionlike dark matter with a liquid-state nuclear spin comagnetometer. *Phys. Rev. Lett.* **2019**, *122*, 191302.

[5] Happer, W.; Tang, H. Spin-exchange shift and narrowing of magnetic resonance lines in optically pumped alkali vapors. *Phys. Rev. Lett.* **1973**, *31*, 273–276.

[6] Wu, T. B.; Xiao, W.; Peng, X.; Wu, T.; Guo, H. Compact high-bandwidth single-beam optically-pumped magnetometer for biomagnetic measurement. *Biomed. Opt. Express* **2025**, *16*, 235–244.

[7] Ma, Y. J.; Yuan, Z. Q.; Lin, S. D.; Zhai, Y. Y.; Tang, J. J. Spin-amplification SERF atomic magnetometer based on direct feedback. *EPJ Quant. Technol.* **2025**, *12*, 70.

[8] Li, H. X.; Lu, Z. W.; Yu, S.; Zhao, M. Y.; Liu, Z. Y.; Li, Z.; Rong, H. W.; Zhang, X. F. High effective permeability and low power loss of FeSiAl/Al_2O_3/ZnO SMC for high frequency application. *Adv. Funct. Mater.* **2024**, *34*, 2403515.

[9] Wang, J.; Li, G. B.; He, Y. H.; Xu, J.; Qiu, Z. G.; Zheng, Z. G.; Xie, M.; Li, Y. Y.; Tian, Y. N.; Liu, X. et al. Improvement in core losses for FeSiAl soft magnetic composites induced by powder annealing treatment. *J. Mater. Res. Technol.* **2023**, *24*, 2500–2513.

[10] Lee, S. K.; Romalis, M. V. Calculation of magnetic field noise from high-permeability magnetic shields and conducting objects with simple geometry. *J. Appl. Phys.* **2008**, *103*, 084904.

[11] Sun, B. W.; Ma, D. Y.; Bai, G. H.; Lu, J. X.; Yang, K.; Wang, K.; Xu, X. P.; Zhai, Y. Y.; Quan, W.; Han, B. C. Correlating the microstructure of Mn–Zn ferrite with magnetic noise for magnetic shield applications. *Ceram. Int.* **2023**, *49*, 11960–11967.

[12] Yan, M.; Yi, S. B.; Fan, X. Y.; Zhang, Z. H.; Jin, J. Y.; Bai, G. H. High-frequency MnZn soft magnetic ferrite by engineering grain boundaries with multiple-ion doping. *J. Mater. Sci. Technol.* **2021**, *79*, 165–170.

[13] Silveyra, J. M.; Ferrara, E.; Huber, D. L.; Monson, T. C. Soft magnetic materials for a sustainable and electrified world. *Science* **2018**, *362*, eaao0195.

[14] Peng, Q.; Ma, M.; Chen, S.; Shi, Y. Q.; He, H. W.; Wang, X. Magnetic-conductive bi-gradient structure design of CP/PGFF/Fe_3O_4 composites for highly absorbed EMI shielding and balanced mechanical strength. *J. Mater. Sci. Technol.* **2023**, *133*, 102–110.

[15] Guo, J.; Li, X.; Chen, Z. R.; Zhu, J. F.; Mai, X. M.; Wei, R. B.; Sun, K.; Liu, H.; Chen, Y. X.; Naik, N. et al. Magnetic $NiFe_2O_4$/polypyrrole nanocomposites with enhanced electromagnetic wave absorption. *J. Mater. Sci. Technol.* **2022**, *108*, 64–72.

[16] Wu, G. H.; Yu, Z.; Guo, R. D.; Wang, Z. G.; Wang, H.; Hu, Z. Q.; Liu, M. Effects of magnetic domain morphology on the magnetic spectrum and high-frequency core losses of MnZn ferrites. *J. Am. Ceram. Soc.* **2024**, *107*, 1117–1126.

[17] Ma, D. Y.; Lu, J. X.; Fang, X. J.; Yang, K.; Wang, K.; Zhang, N.;

Han, B. C.; Ding, M. Parameter modeling analysis of a cylindrical ferrite magnetic shield to reduce magnetic noise. *IEEE Trans. Ind. Electron.* **2022**, *69*, 991–998.
[18] Kornack, T. W.; Smullin, S. J.; Lee, S. K.; Romalis, M. V. A low-noise ferrite magnetic shield. *Appl. Phys. Lett.* **2007**, *90*, 223501.
[19] Shen, P. P.; Zhang, S. Y.; Ma, D. Y.; Xing, B. Z.; Chen, H.; Zhang, M. S.; Wei, H. Q.; Li, B.; Miao, X. Y.; Xie, M. et al. High-shielding coefficient and low-noise of cobalt-based metallic glass magnetic shielding cylinder. *IEEE Trans. Instrum. Meas.* **2025**, *74*, 1004710.
[20] Yang, K.; Lu, J. X.; Ding, M.; Zhao, J. P.; Ma, D. Y.; Li, Y.; Xing, B. Z.; Han, B. C.; Fang, J. C. Improved measurement of the low-frequency complex permeability of ferrite annulus for low-noise magnetic shielding. *IEEE Access* **2019**, *7*, 126059–126065.
[21] Yuan, M. Y.; Zhao, B.; Yang, C. D.; Pei, K.; Wang, L. Y.; Zhang, R. X.; You, W. B.; Liu, X. H.; Zhang, X. F.; Che, R. C. Remarkable magnetic exchange coupling via constructing bi-magnetic interface for broadband lower-frequency microwave absorption. *Adv. Funct. Mater.* **2022**, *32*, 2203161.
[22] Wang, X. Y.; Lv, X. W.; Liu, Z. W.; Zhang, H. B.; Liu, M. M.; Xu, C. Y.; Zhou, X. D.; Yuan, M. Y.; Yang, L. T.; You, W. B. et al. Multi-interfacial 1D magnetic ferrite@C fibers for broadband microwave absorption. *Mater. Today Phys.* **2023**, *35*, 101140.
[23] Chandekar, K. V.; Yadav, S. P. Comprehensive study of MFe_2O_4 (M= Co, Ni, Zn) nanostructures prepared by co-precipitation route. *J. Alloys Compd.* **2023**, *960*, 170838.
[24] Gawas, U. B.; Verenkar, V. M. S.; Vader, V. T.; Jain, A.; Meena, S. S. Effects of sintering temperature on microstructure, initial permeability and electric behaviour of Ni–Mn–Zn ferrites. *Mater. Chem. Phys.* **2022**, *275*, 125250.
[25] Sujatha, C.; Reddy, K. V.; Babu, K. S.; Reddy, A. R.; Rao, K. H. Effect of sintering temperature on electromagnetic properties of NiCuZn ferrite. *Ceram. Int.* **2013**, *39*, 3077–3086.
[26] Martinson, K. D.; Panteleev, I. B.; Steshenko, K. A.; Popkov, V. I. Effect of Bi_2O_3 contents on magnetic and electromagnetic properties of LiZnMn ferrite ceramics. *J. Eur. Ceram. Soc.* **2022**, *42*, 3463–3472.
[27] Ahammed, F.; Khan, M. N. I.; Ullah, M. S.; Badhan, M. A. H.; Sajjad, R. N.; Jamil, A. T. M. K. Influence of microstructure on the magnetic properties of Li–Cu–Mg–Zn ferrites: Role of Bi_2O_3 addition. *J. Magn. Magn. Mater.* **2024**, *606*, 172329.
[28] Hussain, A.; Bai, G. H.; Huo, H. X.; Yi, S. B.; Wang, X. Y.; Fan, X. Y.; Yan, M. Co_2O_3 and SnO_2 doped MnZn ferrites for applications at 3-5 MHz frequencies. *Ceram. Int.* **2019**, *45*, 12544–12549.
[29] Wang, X. Y.; Yi, S. B.; Wu, C.; Bai, G. H.; Yan, M. Correlating the microstructure and magnetic properties of MnZn power ferrites via Co_2O_3 and MoO_3 co-doping for MHz applications. *J. Magn. Magn. Mater.* **2021**, *538*, 168324.
[30] Wu, G. H.; Yu, Z.; Sun, K.; Guo, R. D.; Wang, B.; Jiang, X. N.; Li, L. Z.; Lan, Z. W. Excellent tunable DC bias superposition characteristics for manganese-zinc ferrites. *IEEE Trans. Power Electron.* **2020**, *35*, 1845–1854.
[31] Goodarzi, H.; Sobhani, M. Preparation and properties of CaO-added Mn–Zn ferrite ceramic. *Ceram. Int.* **2023**, *49*, 36700–36705.
[32] Xu, J. F.; Bai, G. H.; Fan, X. Y.; Zhang, Z. H.; Liu, X. L.; Yan, M. Two-step doping of SiO_2 and CaO for high-frequency MnZn power ferrites. *J. Eur. Ceram. Soc.* **2023**, *43*, 2469–2478.
[33] Fan, X. Y.; Bai, G. H.; Zhang, Z. H.; Chen, Q. M.; Jin, J. Y.; Xu, J. F.; Zhang, X. F.; Yan, M. Synergistic effect of V_2O_5 and Bi_2O_3 on the grain boundary structure of high-frequency NiCuZn ferrite ceramics. *J. Adv. Ceram.* **2022**, *11*, 912–921.
[34] Liu, X. B.; Wang, F. F.; Chen, H. J.; Gao, M.; Zhang, H. Fe_2O_3 composition optimization for MnZn ferrite and its magnetic noise evaluation for low-frequency magnetic shielding applications. *J. Alloys Compd.* **2025**, *1035*, 181418.
[35] Guo, H.; Yang, S. F.; Wang, T. T.; Yuan, H.; Zhang, Y. L.; Li, J. S. Microstructure evolution and acicular ferrite nucleation in inclusion-engineered steel with modified MgO@C nanoparticle addition. *J. Mater. Sci. Technol.* **2022**, *99*, 277–287.
[36] Hashim, M.; Ismail, M. M.; Batoo, K. M.; Hadi, M.; Salih, S. J.; Meena, S. S.; Jotania, R. B.; Kumar, N. P.; Naidu, K. C. B.; Shirsath, S. E. Structural, optical, and dielectric properties of $Co_{0.6}Mn_{0.4}Gd_xFe_{2-x}O_4$ ferrites prepared through sonochemical method. *Ceram. Int.* **2024**, *50*, 42677–42685.
[37] Kashkarov, E. B.; Svyatkin, L. A.; Gusev, K. S.; Ognev, S. O.; Koptsev, M.; Terenteva, D. V. Effect of high and low Nb content in multicomponent Nb–Ni–Ti–Zr–Co alloy on its structure, hardness and hydrogen permeability. *Intermetallics* **2024**, *166*, 108180.
[38] Wang, N. C.; Ying, Y.; Zheng, J. W.; Li, W. C.; Qiao, L.; Cai, W.; Li, J.; Che, S. L. Development of Mn–Zn power ferrite with low losses over a broad temperature range for applications in the high frequency region of 0.5–3 MHz. *Ceram. Int.* **2021**, *47*, 21425–21432.
[39] Tokatlidis, S.; Kogias, G.; Zaspalis, V. T. Low loss MnZn ferrites for applications in the frequency region of 1–3 MHz. *J. Magn. Magn. Mater.* **2018**, *465*, 727–735.
[40] Li, Q. F.; Liu, X. Y.; Wang, H.; Lan, Z. W.; Zhang, K.; Wu, C. J.; Liu, P. Y.; Jiang, X. N.; Sun, K.; Yu, Z. Grain-boundary-engineered MnZn ferrites with suppressed power loss and enhanced temperature stability. *Ceram. Int.* **2025**, *51*, 20813–20821.
[41] Han, Y.; Wang, G. W.; Xu, Z. B.; Wang, K.; He, D. L.; Wang, Y.; Wang, T. Fe_4N soft magnetic composite with ultra-low eddy current loss and excess loss above megahertz. *J. Magn. Magn. Mater.* **2024**, *609*, 172467.
[42] Chen, Z. Q.; Geng, Y. F.; Qin, S. Y.; Chen, H.; Chen, L. B.; Tan, J. J.; Chen, X. Z. Fabrication of permalloy with superior magnetic properties using pulsed arc plasma additive manufacturing. *Mater. Today Commun.* **2025**, *46*, 112656.
[43] Ye, X.; Zhang, Z. H.; Bai, G. H.; Fan, X. Y.; Xu, Y. T.; Liu, X. L.; Feng, K. H.; Zhang, X. F. Grain refinement and high-frequency properties of spark plasma sintered MnZn ferrite. *J. Magn. Magn. Mater.* **2024**, *589*, 171487.
[44] Wu, G. H.; Guo, R. D.; Wang, Z. G.; Hu, Z. Q.; Liu, M. Enhanced temperature stability of core losses tuned by Co_2O_3 and YIG ferrite co-doping for MnZn ferrite at 500 kHz. *J. Eur. Ceram. Soc.* **2025**, *45*, 117670.
[45] Xiang, J. C.; Jiang, C. Q.; Ma, T. L.; Wang, X. S.; Fan, Y. S.; Zhou, J. Y. High power density self-resonant coupler for flexible surface wireless power transfer system with nanocrystalline ribbon. *IEEE Trans. Power Electron.* **2024**, *39*, 13975–13987.
[46] Yang, W. D.; Wang, Y. G. Effects of TiO_2 and Co_2O_3 combination additions on the elemental distribution and electromagnetic properties of Mn–Zn power ferrites. *J. Magn. Magn. Mater.* **2015**, *384*, 13–17.
[47] Wang, Z. P.; Wu, P. Y.; Zou, X. B.; Wang, S.; Du, L.; Ouyang, T.; Liu, Z. Q. Optimizing the oxygen-catalytic performance of Zn–Mn–Co spinel by regulating the bond competition at octahedral sites. *Adv. Funct. Mater.* **2023**, *33*, 2214275.
[48] Mugiraneza, S.; Hallas, A. M. Tutorial: A beginner's guide to interpreting magnetic susceptibility data with the Curie-Weiss law. *Commun. Phys.* **2022**, *5*, 95.
[49] Sharma, K.; Aggarwal, N.; Kumar, N.; Sharma, A. A review paper: Synthesis techniques and advance application of Mn–Zn nano-ferrites. *Mater. Today Proc.*, in press, DOI: 10.1016/j.matpr.2022.12.088.
[50] Liu, L. S.; Rojac, T.; Damjanovic, D.; Di Michiel, M.; Daniels, J. Frequency-dependent decoupling of domain-wall motion and lattice strain in bismuth ferrite. *Nat. Commun.* **2018**, *9*, 4928.
[51] Johnson, C.; Schwindt, P. D. D.; Weisend, M. Magnetoencephalography with a two-color pump-probe, fiber-coupled atomic magnetometer. *Appl. Phys. Lett.* **2010**, *97*, 243703.
[52] Wyllie, R.; Kauer, M.; Smetana, G. S.; Wakai, R. T.; Walker, T. G.

Magnetocardiography with a modular spin-exchange relaxation-free atomic magnetometer array. *Phys. Med. Biol.* **2012**, *57*, 2619–2632.

[53] Shah, V. K.; Wakai, R. T. A compact, high performance atomic magnetometer for biomedical applications. *Phys. Med. Biol.* **2013**, *58*, 8153–8161.

[54] Lu, J. X.; Ma, D. Y.; Yang, K.; Quan, W.; Zhao, J. P.; Xing, B. Z.; Han, B. C.; Ding, M. Study of magnetic noise of a multi-annular ferrite shield. *IEEE Access* **2020**, *8*, 40918–40924.

[55] Gao, Y. N.; Ma, D. Y.; Li, M. C.; Zhang, M. S.; Chen, Y. B.; Han, C. M.; Wang, Y. T.; Fang, X. J.; Dou, Y.; Wang, K. Analysis and measurement of magnetic noise for tesla shielding based on superconducting coils applied to SERF magnetometer. *Measurement* **2025**, *242*, 115971.

[56] Dang, H. B.; Maloof, A. C.; Romalis, M. V. Ultrahigh sensitivity magnetic field and magnetization measurements with an atomic magnetometer. *Appl. Phys. Lett.* **2010**, *97*, 151110.

[57] Sulai, I. A.; DeLand, Z. J.; Bulatowicz, M. D.; Wahl, C. P.; Wakai, R. T.; Walker, T. G. Characterizing atomic magnetic gradiometers for fetal magnetocardiography. *Rev. Sci. Instrum.* **2019**, *90*, 085003.

[58] Li, Y.; Liu, X. J.; Cai, H. W.; Ding, M.; Fang, J. C. Optimization of the alkali-metal density ratio in a hybrid optical pumping atomic magnetometer. *Meas. Sci. Technol.* **2019**, *30*, 015005.

[59] Sun, B. W.; Ma, D. Y.; Fang, X. J.; Xue, Y. Z.; Lu, J. X.; Chen, H.; Zhang, M. S.; Wei, H. Q.; Han, B. C.; Zhai, Y. Y. Suppression of magnetic noise and field in cubic low-noise ferrite magnetic shields. *IEEE Trans. Instrum. Meas.* **2024**, *73*, 1501810.